

Supplementary Material: Channel Dynamics in an Experimental Alluvial Fan Under Constant Boundary Conditions: A Classification of Avulsion and Lateral Migration Events

Nastaran Nematollahi^{1, 2}, Brett Eaton^{1, 2}, and Sarah Davidson^{1, 2}

¹Department of Geography, University of British Columbia, 1984 West Mall, Vancouver, BC V6T 1Z2, Canada

²BGC Engineering Inc., 980 Howe Street, Vancouver, BC V6Z 0C8, Canada

Correspondence: Nastaran Nematollahi (nasipour@student.ubc.ca)

1 Supplementary Methods: Detailed Description

Here we provide additional details about the equipment, data sources, and preprocessing steps used in the experiment. Specifically, we describe the camera setup, the two datasets collected (3D photogrammetry images and high-frequency RGB images), and the methods applied to prepare these datasets for analysis.

5 S1.1 Equipment

A total of seven Canon EOS Rebel T6i DSLRs were used in the experiment. One camera was mounted directly overhead, 1.5 m above the center of the fan surface, oriented vertically downward, and captured RGB images at 3-second intervals to document surface flow patterns at high spatial and temporal resolution. The remaining six cameras were dedicated to Structure-from-Motion (SfM) photogrammetry for generating digital elevation models (DEMs). These cameras were mounted side-by-side on
10 a rigid rail system positioned 1.0 m above the fan table. The rail was moved in 10 cm increments along the 2.5 m table length, and at each stop all six cameras were triggered simultaneously, producing 78 photographs per DEM acquisition. Based on the APS-C sensor size (22.3×14.9 mm), focal length of 18 mm, and camera height of 1.0 m, each image covered a ground footprint of $\sim 1.2 \times 0.8$ m, yielding a ground sampling distance of ~ 0.24 mm/pixel and forward overlap of 88–92%. Photogrammetry image sets were collected every 30 minutes, after water flow had stopped and the fan surface had drained, ensuring a static,
15 reflection-free bed. Camera positions are shown in the main manuscript (fig.S1).

We conducted photogrammetry in Agisoft Photoscan Professional (Version 1.4.5, build 7354). The image sets were processed using high-quality settings for image alignment and aggressive filtering to generate dense topographic point clouds. Each dense cloud contained over 11 million points, yielding an average density of approximately 3.4 million points per square meter, equivalent to a mean point spacing of ~ 0.55 mm. From these point clouds, we produced DEMs at 0.5 mm/pixel
20 resolution.

All cameras were identical Canon EOS Rebel T6i DSLRs equipped with Canon EF-S 18–55 mm lenses fixed at 18 mm focal length. They were set to an aperture of $f/10$ and ISO 400, with focus adjusted manually before each experiment and autofocus

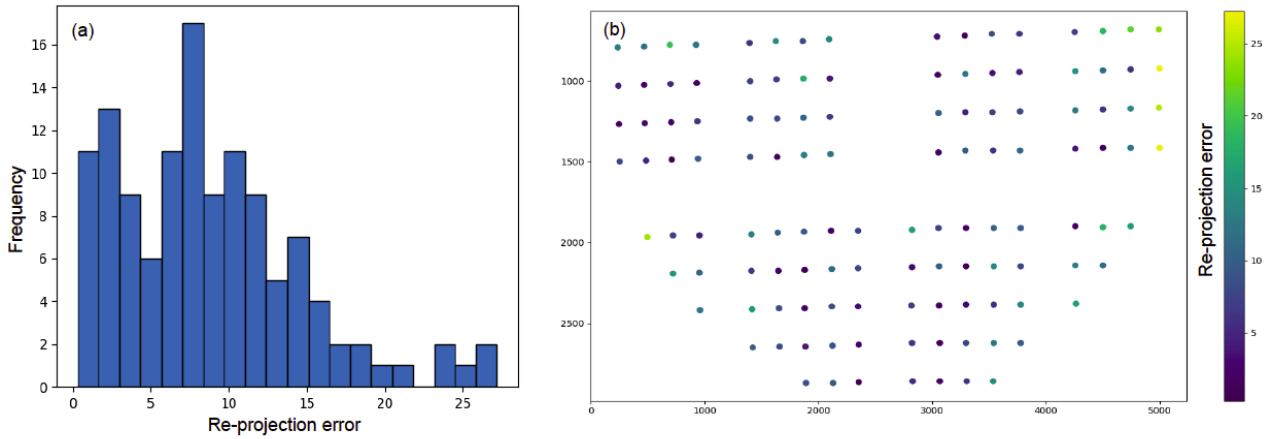


Figure S1. Distribution of re-projection errors following homography-based image transformation.

disabled to maintain consistency. Illumination was provided by two LED lights positioned at the downstream corners, while a translucent plastic sheet covered the setup to reduce glare from ceiling lights and daylight, ensuring uniform lighting and minimal shadowing across image sequences.

S1.2 Image preprocessing

Image preprocessing steps—including georectification, georeferencing, fan surface masking—and optical flow analyses were performed in Python using the OpenCV library (Bradski, 2000). All other analyses, including raster calculations and spatial analysis, were conducted in R using the Terra package (R Core Team, 2025; Hijmans, 2024). All scripts, along with a representative subset of the experimental dataset and animated videos of the experiment, are available in our GitHub repository.

S1.2.1 Image georectification and georeferencing

We corrected the radial distortion of the overhead Canon DSLR camera, which was installed for flow mapping, using Adobe Photoshop’s Auto Lens Correction feature, which considers the camera-specific EXIF metadata to apply the appropriate distortion profile. Further, all the rectified images were georeferenced to our defined coordinate system using a reference orthophoto through a homography-based transformation. The accuracy of this alignment was calculated using the mean reprojection error—defined as the Euclidean distance between transformed points in the corrected image and their corresponding locations in the orthophoto—which was 10.11 pixels, equivalent to 10 *mm*. As shown in Figure S1 (b), the high values of reprojection errors are related to the left and right corners of the image beyond the maximum fan extent. An overlay of the transformed image on the reference orthophoto is presented in Figure S2.

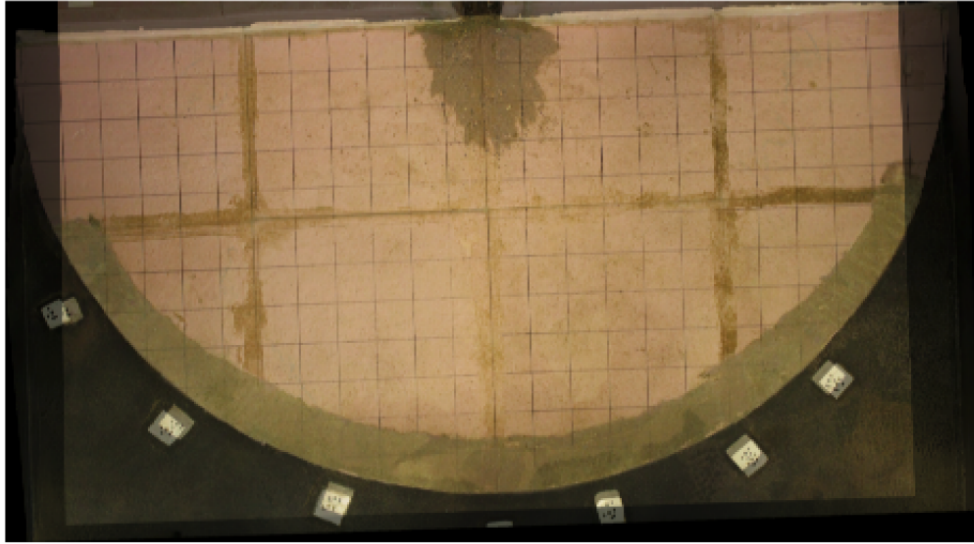


Figure S2. Overlay of orthophoto and transformed image post homography application.

40 **S1.2.2 Fan surface masking**

The overhead camera used to capture flow images had a wider field of view than the fan, including parts of the experimental setup and the sheet beneath the fan. To isolate the fan surface, we first applied a Gaussian blur with $\sigma = 5$ to reduce noise caused by grain texture and lighting variability. We then performed intensity thresholding using a value ranging from 112 to 117, which was empirically determined and visually inspected at regular intervals (every 600 images) to account for minor lighting changes over time. We further refined the resulting binary mask using a morphological erosion operation with a 3×3 kernel to eliminate small, isolated noise elements, as shown in Figure S3. The final binary mask was applied to each frame to isolate the active fan surface. These masked images were then used to calculate fan area and fan radius through time and to compile video sequences for optical flow analysis.

To assess how well the optical flow method identifies geomorphically active areas, we compared cumulative pixel-motion maps generated over 30-minute intervals with Difference of DEMs (DoDs), calculated between successive DEMs taken at the beginning and end of each interval. As shown in Figure S4 (a) and (b), the sensitivity of the optical flow method—measured as the proportion of true geomorphic changes (identified by the DoD) that were correctly detected—remained consistently high, often exceeding 0.90. In contrast, the precision—measured as the proportion of optical flow detections that corresponded to true geomorphic changes approximately $51\% \pm 2.7\%$. Precision was highest during the early stages of the experiment and gradually declined in later phases, which can be attributed to the fan's lateral expansion into regions of the table with greater photogrammetric distortion and reprojection error.

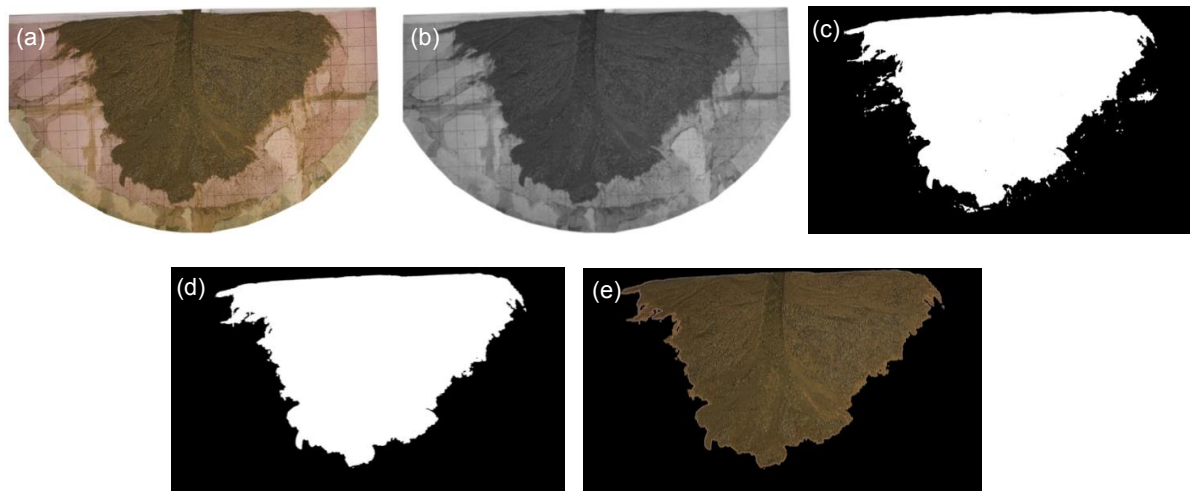


Figure S3. Preprocessing steps for isolating the fan surface. (a) Georeferenced and georectified image. (b) Smoothed image after applying a Gaussian blur filter. (c) Binary mask obtained through intensity-based thresholding. (d) Refined mask following a morphological erosion operation. (e) Final masked fan surface overlaid on the original image.

Some of the observed differences between the geomorphically active areas derived from optical flow and those derived from DoD are also related to ephemeral scour–fill cycles. These are short-lived processes in which water temporarily erodes a slight depression (scour) and deposits sediment into the same location (fill), resulting in negligible net elevation change. While the DoD captures only the net effect—often showing no change—the algorithm captures any pixel-level motion (change in intensity), including those that are reversed within minutes. Consequently, the cumulative flow maps may record surface activity that ultimately leaves no morphologic trace in the DEMs. From a geomorphological perspective, such ephemeral motion is important, as it reflects sediment transport dynamics, sorting, or channel reworking that precedes more permanent morphological adjustments. Thus, this discrepancy between optical flow and DoD is not necessarily a limitation but a complementary view: DoDs capture the outcome of change, while optical flow reveals the process. Together, they provide information about where and when the fan surface is in motion and whether that motion ultimately results in lasting morphodynamic change.

Although the 3-second frame interval allowed detection of broader zones of surface activity, it was insufficient to detect the displacement of individual grains. Moreover, because optical flow estimates apparent motion based on intensity changes rather than physical tracking of mass, the resulting flow fields do not represent true velocity fields. As noted by Liu and Shen (2008), the brightness constancy assumption foundational to optical flow is not derived from physical laws and may be violated by lighting changes, sediment disturbance, and water-surface reflections. Therefore, while optical flow provides a useful proxy for identifying zones of geomorphic activity, quantitative interpretation of displacement magnitudes would require independent calibration against known physical motion.

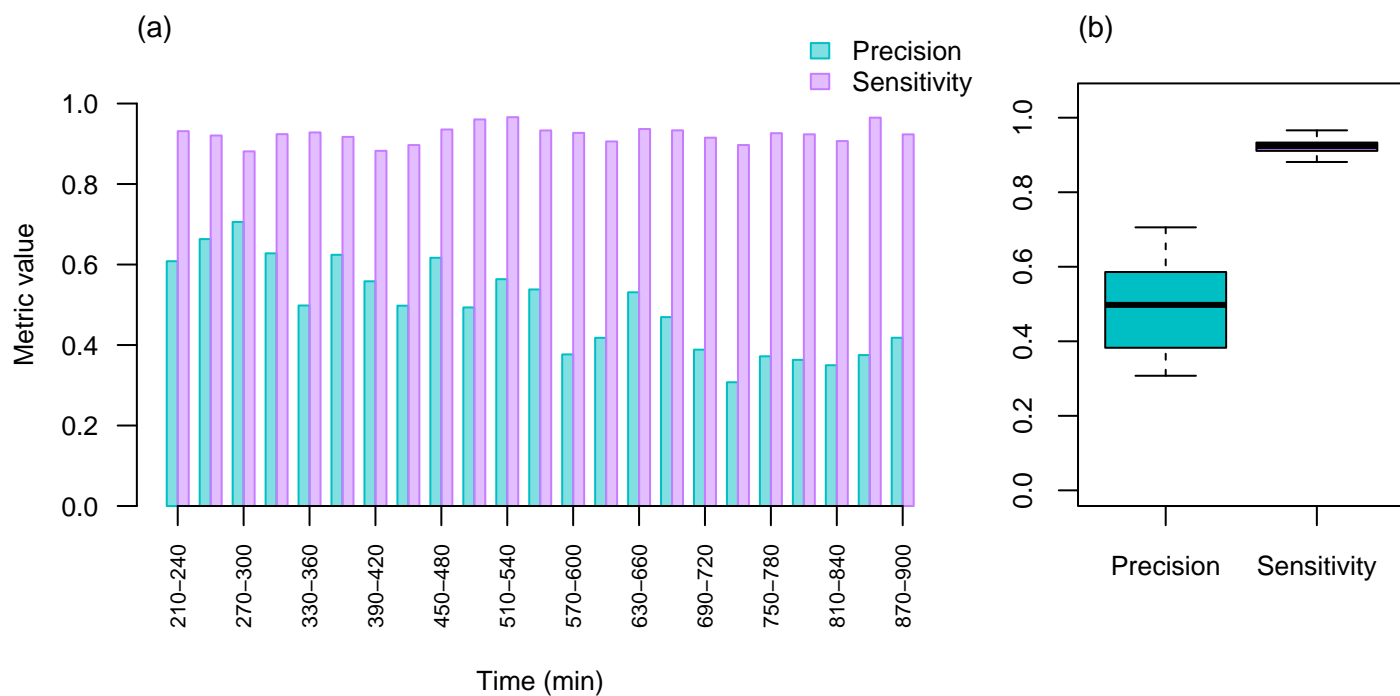


Figure S4. (a) Precision and sensitivity over time, compared to geomorphic change from DoDs. (b) Boxplots showing distributions across all intervals.

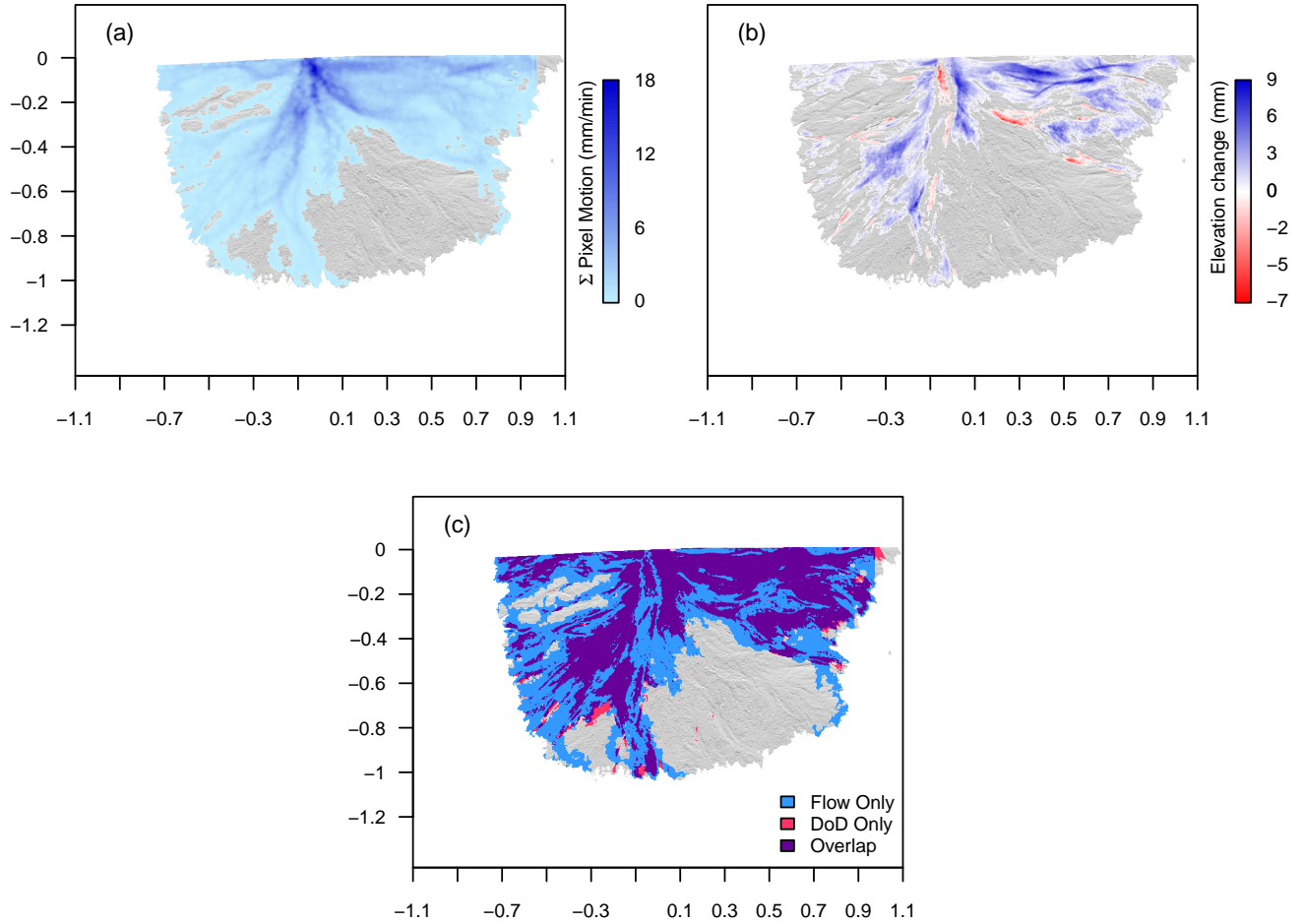


Figure S5. Comparison of active flow areas using (a) cumulative pixel motion from optical flow over 30 minutes of the experiment, indicating water and sediment movement, and (b) Difference of DEMs (DoD), showing sediment redistribution.

75 2 Supply-Limited and Transport-Limited Phases

Although discharge and sediment supply were held constant during the experiment, the local balance between sediment supply and transport capacity appeared to vary as the channel network reorganized. Because direct measurement of sediment flux or local transport capacity was not feasible in our small-scale physical model, these states were inferred from channel-network configuration, mobility, and reorganization style.

80 To support this interpretation, we used three channel-network metrics derived from the channel detection procedure described in Section 2.2.2 of the main manuscript: the number of active channel threads, the TMC ratio, and the angular spread of the active network. Together, these metrics describe whether the channel network was relatively simple and structured, with activity concentrated in one or a few dominant channels, or more complex and distributed across multiple active threads.

Number of active channel threads (n_{channels}). This metric records the number of active channel threads detected at each
85 time step. A high value indicates a more distributed, multi-thread network, whereas a low value indicates activity concentrated in one or two dominant threads.

TMC ratio. The Total Motion Contribution (TMC) of a single channel thread i is defined as the product of the mean pixel-wise optical-flow magnitude within that channel and its total length:

$$\text{TMC}_i = \bar{v}_i \times L_i$$

90 where \bar{v}_i is the mean flow magnitude (pixel units per frame) and L_i is the channel length (pixels). TMC combines the relative motion intensity and length of each channel thread, and is used here as a proxy for the relative contribution of each thread to total network activity. The TMC ratio is then defined as the TMC of the dominant (highest-TMC) channel divided by the sum of TMC across all active channel threads:

$$\text{TMC ratio} = \frac{\max_i(\text{TMC}_i)}{\sum_i \text{TMC}_i}$$

95 A value close to 1.0 indicates that most network activity is concentrated in a single dominant channel. Lower values indicate that activity is distributed more evenly across multiple active threads. The TMC ratio is bounded between $1/n_{\text{channels}}$ (perfectly equal distribution) and 1.0 (full concentration in one thread).

Angular spread. This metric quantifies how broadly the channel network fans across the fan surface, measured as the angular range subtended by the full network from the upstream apex. For each channel pixel at coordinates (X, Y) , the bearing
100 angle from the upstream-most channel point (the apex, at coordinates X_0, Y_0) is computed as:

$$\theta = \arctan\left(\frac{X - X_0}{-(Y - Y_0)}\right) \times \frac{180}{\pi}$$

The sign convention follows the standard compass bearing (positive values to the right of the apex, negative to the left), and the minus sign in the denominator accounts for the fact that the Y -axis increases downward in image coordinates. The angular spread is then the range of these angles across all channel pixels: $\max(\theta) - \min(\theta)$. A wide angular spread indicates that the active network occupies a broad portion of the fan surface, whereas a narrow angular spread indicates that activity is confined to a more limited corridor.

Because the three metrics are measured in different units and on different scales, each was standardized to a z-score before combining:

$$z(x) = \frac{x - \bar{x}}{\sigma_x}$$

where \bar{x} and σ_x are the mean and standard deviation across all time steps. The TMC ratio was inverted before standardization, $z(-\text{TMC ratio})$, so that all three standardized metrics vary in the same direction. Higher values therefore indicate a more complex and distributed channel network. The composite complexity index was then defined as:

$$\text{Complexity Index} = z(n_{\text{channels}}) + z(-\text{TMC ratio}) + z(\text{angular spread})$$

We applied k-means clustering to the three standardized metrics simultaneously. The elbow plot was used to compare solutions with $k = 1$ to 8 clusters. The hidden chunk below loads the data and computes the z-scores used throughout this section:

The elbow plot (Figure S6) shows a sharp drop in WSS from $k = 1$ to $k = 2$, with each additional cluster beyond $k = 2$ providing only marginal improvement. We therefore used $k = 2$ (50 random initialisations, fixed seed `set.seed(42)` for reproducibility) to separate the record into two recurring channel-network states. No threshold on any individual metric was imposed; the boundary was defined from the multivariate clustering.

The cluster with more active channel threads, lower TMC ratio, and wider angular spread was interpreted as a relatively transport-limited state. In this state, activity was distributed across multiple threads, consistent with greater sediment storage and reworking across the mid-fan.

The cluster with fewer active channel threads, higher TMC ratio, and narrower angular spread was interpreted as a relatively supply-limited or efficiently connected state. In this state, activity was concentrated in one or a few dominant channels, consistent with more efficient sediment routing toward the fan toe.

These terms are interpretive. Sediment flux, stream power, and local transport capacity were not measured directly in this experiment. The supply-limited and transport-limited states are therefore inferred from channel-network geometry and optical-flow activity patterns rather than from direct sediment-flux measurements.

The code chunk below shows how the three metrics were extracted from the optical flow CSV files for each time step (provided for reproducibility, not evaluated at compile time):

The following hidden chunk applies k-means with $k = 2$ and defines all helper functions used by the figures below:

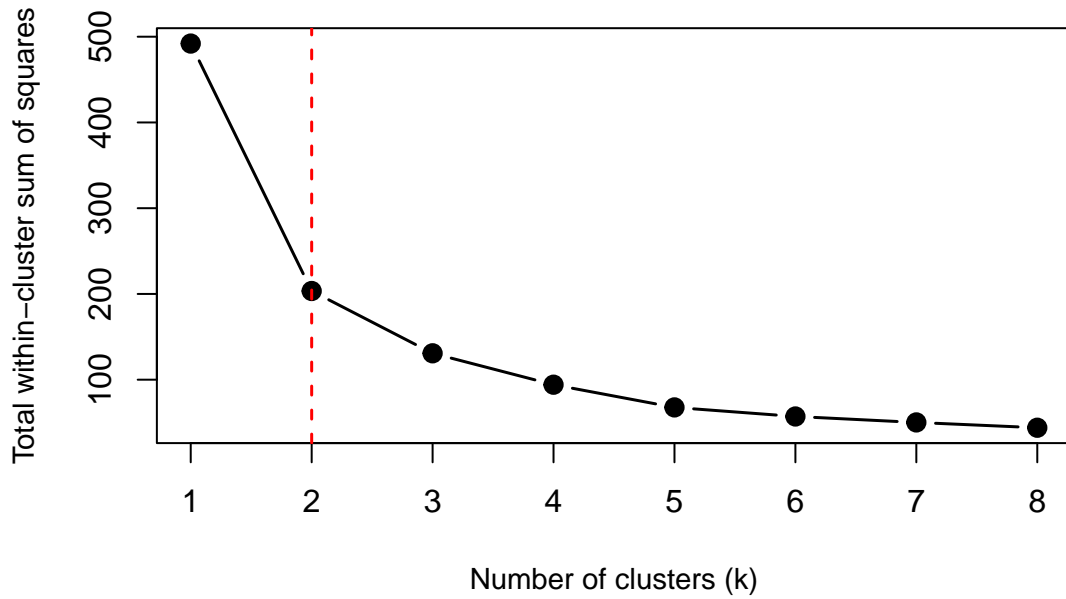


Figure S6. Elbow plot showing the total within-cluster sum of squares (WSS) for k-means solutions with $k = 1$ to 8 clusters, applied to the three standardized channel-network metrics. The largest reduction in WSS occurs between $k = 1$ and $k = 2$. The dashed red line marks $k = 2$, the solution used to separate the record into two recurring channel-network states.

S2.1 Raw metric time series

Figure S7 shows how each of the three raw metrics changed through the 328-minute analysis window. Even before any classification is applied, all three metrics display a coherent alternating structure: intervals with many channels, low TMC ratios, and wide angular spreads are interspersed with intervals of one or two channels, high TMC ratios, and narrow angular spreads. The transitions are often abrupt — occurring within one or two 2-minute time steps — and are consistent in timing across all three metrics. This cross-metric coherence suggests that the three variables are capturing the same underlying shift in channel-network configuration.

Figure S8 shows the k-means clustering result projected onto all three pairwise combinations of the standardized metric axes. Each point represents one 2-minute time step, coloured by its assigned state. The cluster centres are shown as large star symbols. The two clusters are cleanly separated in all three pairwise projections, indicating that the two-cluster structure is consistent across the three metric projections. The relatively transport-limited cluster consistently occupies the upper-right corner of each panel (high $z(n_{\text{channels}})$, high $z(-\text{TMC ratio})$, high $z(\text{angular spread})$), while the relatively supply-limited cluster occupies the lower-left corner.

Figure S9 repeats the raw metric time series from Figure S7, but with each point now coloured by its assigned state and with semi-transparent background bands highlighting the extent of each interval. Red points and red shading indicate relatively transport-limited intervals, when the network was more complex and distributed. Blue points and blue shading indicate rel-

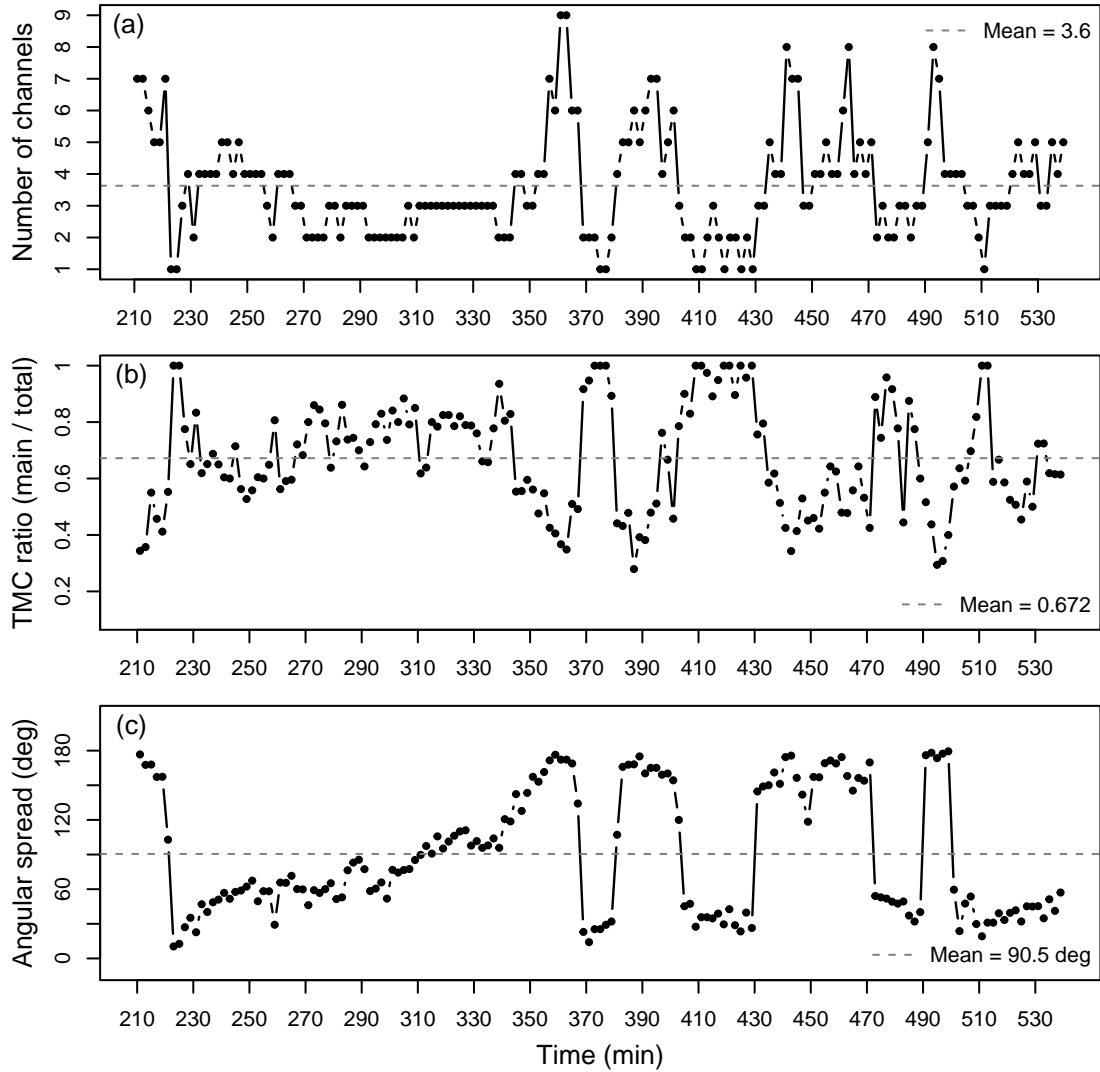


Figure S7. Time series of the three raw channel-network metrics across all 165 two-minute time steps (minutes 211–539). (a) Number of simultaneously active channel threads. (b) TMC ratio: the fraction of total network activity carried by the dominant channel thread; values near 1 indicate a single dominant channel, while lower values indicate that activity is distributed across multiple threads. (c) Angular spread: the full angular range subtended by the channel network as seen from the upstream apex. The dashed horizontal line in each panel marks the grand mean of that metric across all time steps. The alternating pattern visible in all three panels reflects recurring transitions between a more complex, distributed configuration (interpreted as relatively transport-limited) and a simpler, more consolidated configuration (interpreted as relatively supply-limited or efficiently connected).

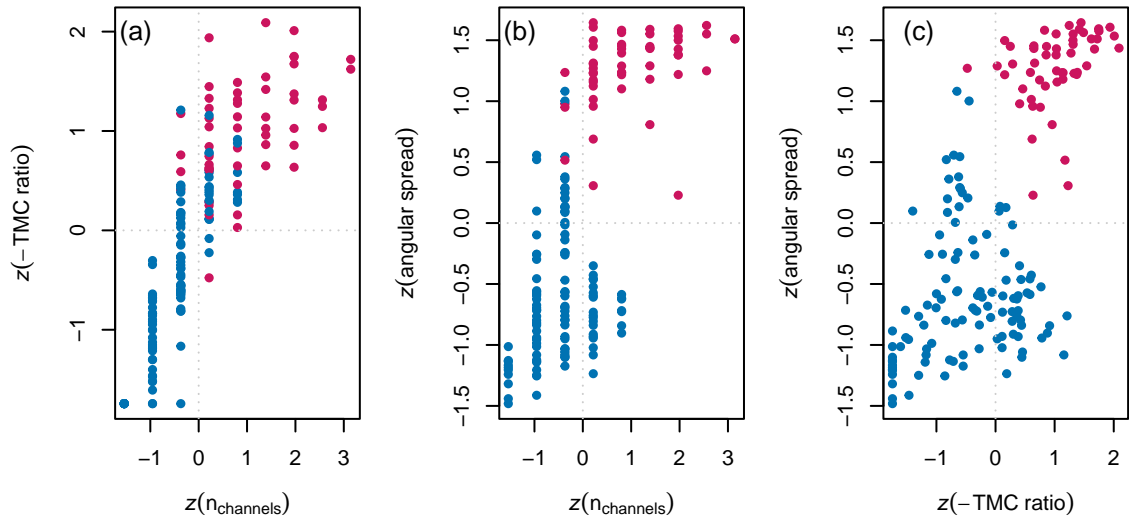


Figure S8. K-means clustering result projected onto all three pairwise combinations of standardized metric axes. Each point is one 2-minute time step, coloured by assigned state: red/tomato = relatively transport-limited; blue = relatively supply-limited or efficiently connected. Star symbols mark the k-means cluster centres. The clean separation in all three panels indicates that the two-cluster structure is consistent across the three metric projections.

atively supply-limited or efficiently connected intervals, when activity was concentrated in one or a few dominant channels. The consistent alignment between point colour and metric value across all three panels indicates that the same time steps are
150 classified consistently across all three metrics.

Figure S10 shows the composite complexity index through time. Because the index is the additive sum of three z-scored metrics that all respond coherently to the same underlying transition, it amplifies the contrast between the two states relative to any single metric. The index oscillates above and below zero (the grand mean), with strongly positive values when the network is complex and distributed and strongly negative values when the network is simple and consolidated. The transitions stand out
155 clearly as crossings of the zero line, making the index a convenient single-variable summary of channel-network state. This is the variable whose time series (with state shading) is presented in the main manuscript Results section.

Figure S11 shows boxplots of each raw metric separately for the two states. Individual time-step values are overlaid as jittered points to show the full distribution, not just the quartile summary. All three metrics show clear separation between states in the expected directions: relatively transport-limited time steps have more active channel threads, lower TMC ratios,
160 and wider angular spreads than relatively supply-limited time steps. This indicates that the k-means classification captures an internally consistent distinction between the two channel-network states.

We emphasize that these interpretations are based on channel-network geometry and optical-flow activity patterns. Transport rates and stream power were not measured directly, so the terms supply-limited and transport-limited should be read as inferred sediment-routing states rather than direct measurements of sediment flux or transport capacity.

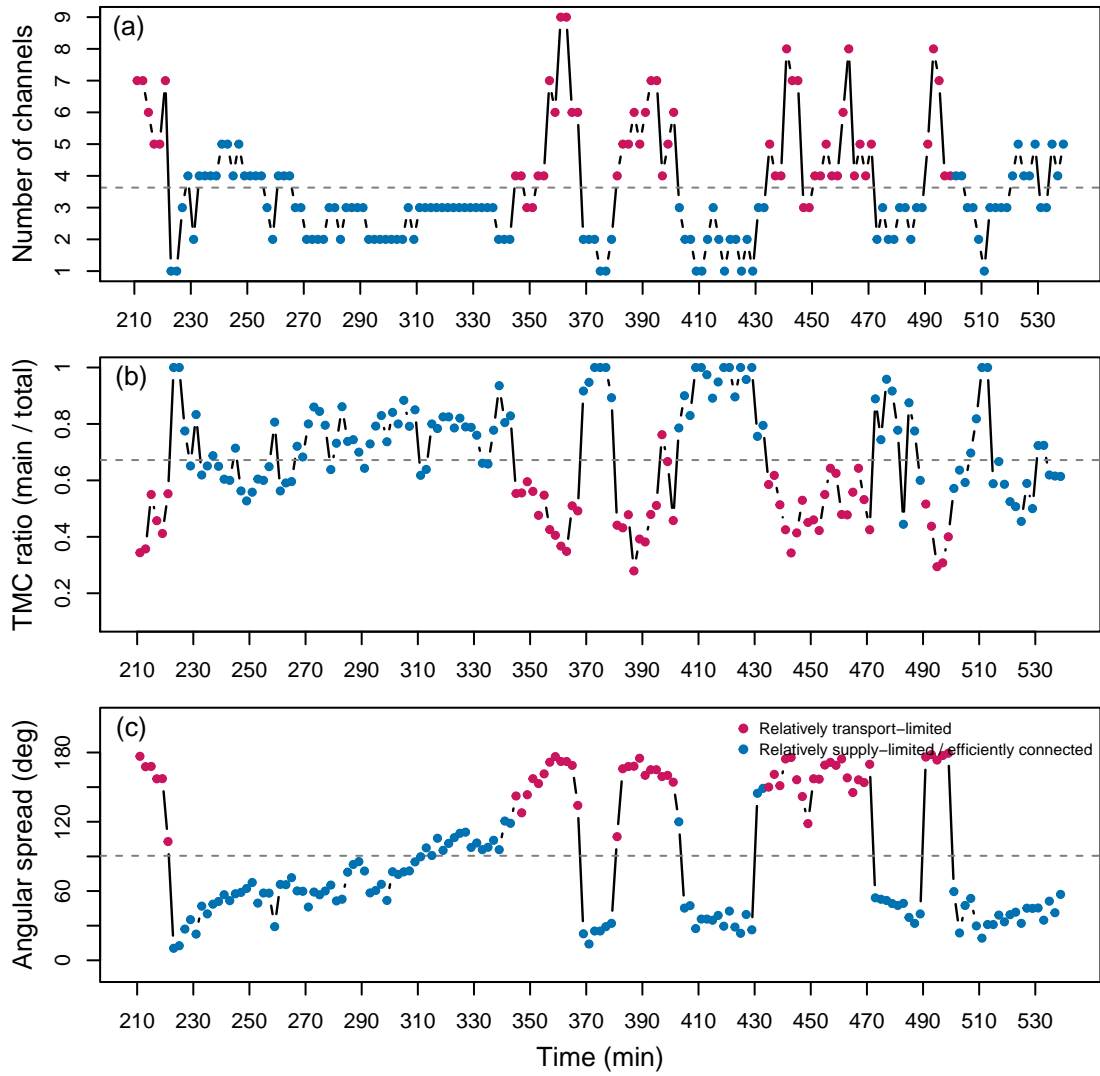


Figure S9. Time series of the three channel-network metrics coloured by assigned state. Red points and red shading indicate relatively transport-limited intervals, when the network was more complex and distributed. Blue points and blue shading indicate relatively supply-limited or efficiently connected intervals, when activity was concentrated in one or a few dominant channels.

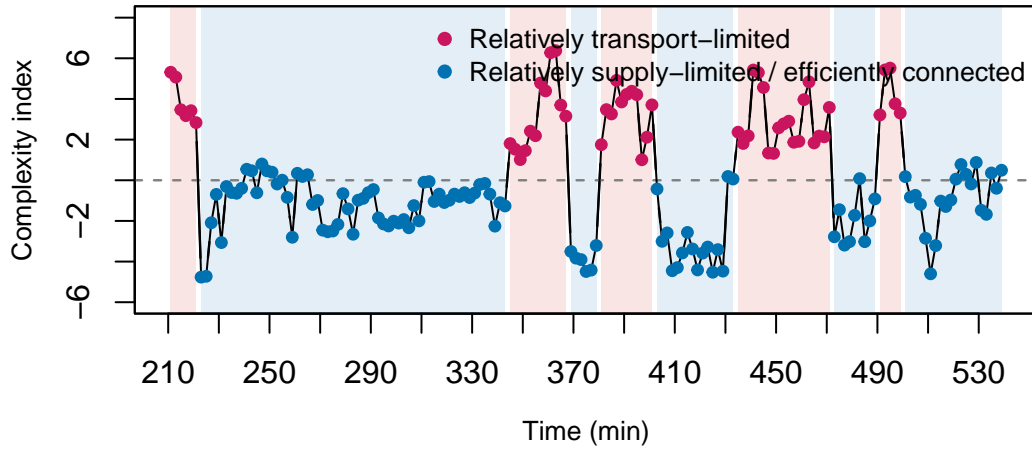


Figure S10. Composite channel-network complexity index through time, coloured by assigned state. The index is the additive sum of three standardized metrics: $z(n_{\text{channels}}) + z(-\text{TMC ratio}) + z(\text{angular spread})$. Positive values indicate a more complex and distributed network, interpreted as relatively transport-limited (red points and red shading). Negative values indicate a simpler and more consolidated network, interpreted as relatively supply-limited or efficiently connected (blue points and blue shading). The dashed horizontal line marks zero (the grand mean across all time steps).

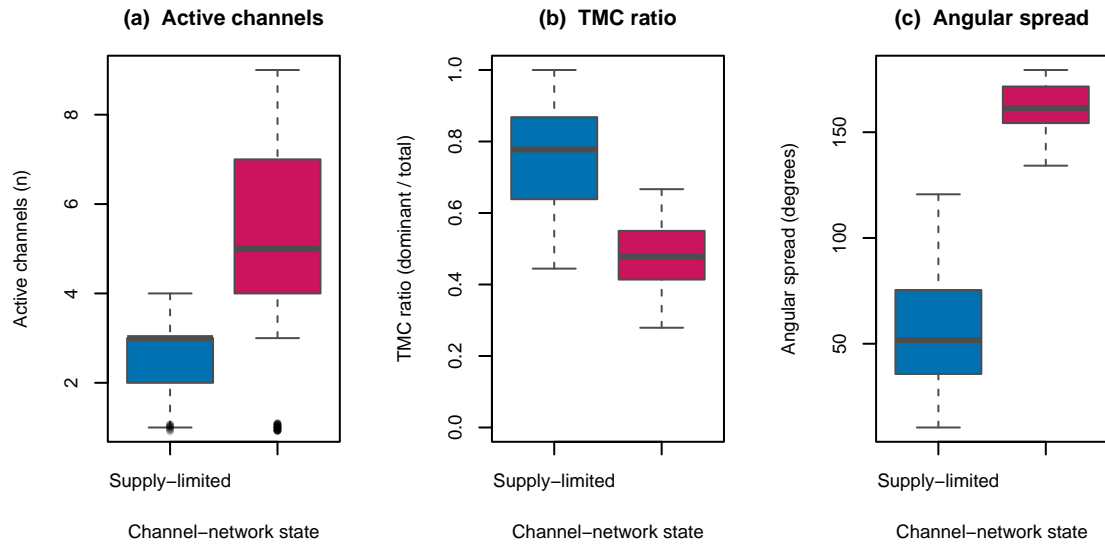


Figure S11. Distributions of the three raw channel-network metrics by assigned state. 'Supply-limited' on the x-axis refers to the relatively supply-limited or efficiently connected state. 'Transport-limited' refers to the relatively transport-limited state. Box = interquartile range; central line = median; whiskers = $1.5 \times \text{IQR}$; jittered points show individual 2-minute time steps. Blue = supply-limited; red/tomato = transport-limited. All three metrics show separation between states in the expected directions.

165 *Code and data availability.* The full source data for this study exceed 1 TB in size and are therefore not hosted online. Code and sample data are openly available at: <https://github.com/Nastarannmt>. The complete datasets are available from the corresponding author upon reasonable request.

Video supplement. The supplementary video presents a time-lapse sequence from 210 to 540 minutes of the 9-hour experiment. The initial 3.5 hours, during which the fan developed its baseline morphology, are excluded. The video therefore focuses on the period analyzed in the
170 study, capturing the active phases of channel migration, reorganization, and avulsion.

Author contributions. NN designed and carried out the experiments, processed optical-flow maps and DEMs, analyzed results, and drafted the manuscript. BRE supervised the study, contributed to interpretation, and edited the manuscript. SD provided technical guidance and contributed to analysis and manuscript revisions.

Competing interests. The authors declare no competing interests.

175 *Disclaimer.* The authors used AI-assisted proofreading tools to improve grammar and clarity. All interpretations and conclusions are solely those of the authors.

Acknowledgements. Experimental construction and equipment purchase were supported by an NSERC Discovery Grant awarded to B. Eaton. N. Nematollahi was supported by a Four Year Doctoral Fellowship from the University of British Columbia. We thank Anya Leenman for her in-depth reviews, which greatly improved the clarity and quality of the manuscript.

180 **References**

Bradski, G.: The OpenCV Library, in: Dr. Dobb's Journal of Software Tools, 2000.

Hijmans, R. J.: terra: Spatial Data Analysis, <https://cran.r-project.org/package=terra>, r package version 1.7-78, 2024.

Liu, T. and Shen, L.: Fluid flow and optical flow, Journal of Fluid Mechanics, 614, 253–291, <https://doi.org/10.1017/S0022112008003273>, 2008.

185 R Core Team: R: A Language and Environment for Statistical Computing, R Foundation for Statistical Computing, Vienna, Austria, <https://www.R-project.org/>, 2025.